Journal of Hazardous Materials 402 (2021) 123498

Contents lists available at ScienceDirect

Journal of Hazardous Materials

journal homepage: www.elsevier.com/locate/jhazmat

Two-dimension N-doped nanoporous carbon from KCl thermal exfoliation of Zn-ZIF-L: Efficient adsorption for tetracycline and optimizing of response surface model

Haihao Peng[a,b,1], Jiao Cao[a,b,1], Weiping Xiong[a,b,*], Zhaohui Yang[a,b,*], Meiying Jia[a,b], Saiwu Sun[a,b], Zhengyong Xu[c], Yanru Zhang[a,b], Hongchun Cai[d]

[a] College of Environmental Science and Engineering, Hunan University, Changsha 410082, PR China
[b] Key Laboratory of Environmental Biology and Pollution Control (Hunan University), Ministry of Education, Changsha 410082, PR China
[c] Science and Technology Service Center of Hunan Province, Changsha 410128, PR China
[d] Hunan Xinheng Environmental Technology Co Ltd, Changsha 410005, PR China

GRAPHICAL ABSTRACT

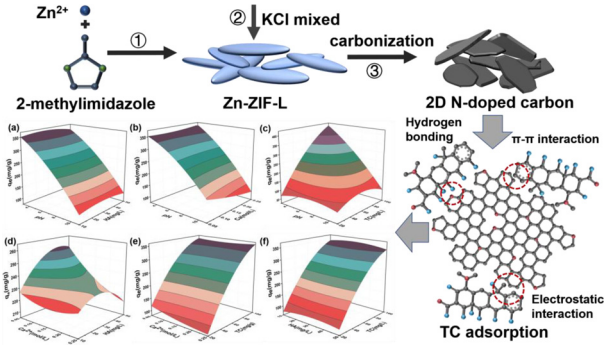

ARTICLE INFO

Keywords:
N-doped nanoporous carbon
Two-dimensional
Adsorption
Tetracycline
Response surface model

ABSTRACT

N-doped nanoporous carbon (NC) with two-dimensional structure derived from Zn-ZIF-L via KCl exfoliation and carbonization at different temperature were prepared for adsorptive removal of tetracycline (TC). Characterizations revealed the effective dopant of N atoms and low degree of graphitization with more defects related to the enhanced adsorption capacity of the NC materials. Benefiting from the huge surface area (2195.57 $m^2\ g^{-1}$), high porosity (1.34 $cm^3\ g^{-1}$) and accessible sheeting structure, the NC-800 exhibited its fast and efficient adsorption of TC in 60 min. Meantime, the maximum adsorption of TC could reach 347.06 mg g^{-1}. Effects of pH, humic acid (HA) and ionic strength (Na^+, Ca^{2+}) were studied along with the interactions among influencing factors investigated by response surface model (RSM). By optimizing experimental conditions from RSM, the adsorption capacity could increase to 427.41 mg g^{-1}. Additionally, electrostatic interaction and hydrogen bond interaction might play a dominating role in adsorption reaction. The NC-800 could maintain a high adsorption level after four cycles. Therefore, the NC-800 with great adsorptive property and reusability could be considered as an effective adsorbent with promising potential in applications for water treatment.

* Corresponding authors at: College of Environmental Science and Engineering, Hunan University, Changsha Hunan 410082, PR China.
E-mail addresses: xiongweiping@hnu.edu.cn (W. Xiong), yzh@hnu.edu.cn (Z. Yang).
[1] These authors contribute equally to this article.

https://doi.org/10.1016/j.jhazmat.2020.123498
Received 7 April 2020; Received in revised form 10 July 2020; Accepted 12 July 2020
Available online 16 July 2020
0304-3894/

1. Introduction

Antibiotics had been used widely in medical treatment for humankind and animals (Cetecioglu et al., 2013). On account of effective bacteriostasis and being easy to acquire, the abuse of antibiotics led to severe water environment pollution (Gao et al., 2012; Xu et al., 2019a). Recent research found that the concentration level of antibiotics could reach to μg L^{-1} in natural waters and the concentration in medical wastewater even to mg L^{-1} (Zhang et al., 2015; Cao et al., 2018). Among various antibiotics, tetracycline (TC) was one of the most used all over the world since it possessed broad-spectrum antibacterial property (Wang et al., 2018). Actually, it was hard to degrade or eliminate TC completely in conventional water treatment process by reason of high stability and low biodegradability (Jia et al., 2020; Xu et al., 2017). On the other hand, the second pollution generating from TC tended to be more toxic and should be noticeable (Liu et al., 2019; Bai et al., 2019).

So far, there were numerous methods being employed for TC removal, mainly including advanced oxidation, photocatalytic, biodegradation, membrane separation and adsorption. Among them, adsorption was a simple but efficient solution owning to relatively inexpensive cost, easy to operate and high removal efficiency (Sarker et al., 2017a). As for adsorption process, performances of adsorbents would be one determining factor during adsorption reaction. A large number of researchers fixed their attention on carbonaceous materials, such as graphene oxide, activated carbon, carbon nanotubes, and nanoporous carbon (Huizar Felix et al., 2019; Jiang et al., 2016; Cao et al., 2020a). For instance, Carabineiro et al. investigated the adsorption of ciprofloxacin using activated carbon, carbon xerogel and carbon nanotubes. By surface modification of these carbon materials, the adsorption capacities got improved and could reach 300 mg g^{-1} (Carabineiro et al., 2011; Carabineiro et al., 2012). Metal-organic frameworks (MOFs) belonged to porous materials made up of metal centers and organic linkers (Cao et al., 2020b). Particularly, nanoporous carbon derived from MOFs showed superior performances and had become a new research focus in many fields. The nanoporous carbon retained the properties of MOFs with large surface area and ordered porous structure. Besides, it possessed higher thermal and chemical stability in comparison to original MOFs, which could extend its application range even in some adverse circumstances, such as overly acidic or alkaline and other complex conditions. Torad et al. synthesized Co-doping nanoporous carbon particles (Co/NPC) derived from ZIF-67 with excellent adsorption performance for methylene blue (MB). The high nanoporosity and well-developed graphitized wall of Co/NPC achieved fast-diffusion of MB molecules and accessibility of Co nanoparticles (Torad et al., 2014). Moreover, the doping of nitrogen into nanoporous carbon could improve the performance of materials via changing surface properties and adjusting channel structures (Bhadra et al., 2019). Sarker and his partners prepared nitrogen-doped porous carbon by carbonizing the compounds of ionic liquid and ZIF-8. The obtained porous carbon exhibited remarkable adsorption capacities for diuron (284 mg g^{-1}) and 2, 4-dichlorophenoxyacetic acid (448 mg g^{-1}). It could be ascribed to the active sites provided by surface nitrogen/oxygen species as well as its own high porosity (Sarker et al., 2017b).

Recently, two-dimension carbonaceous materials had drawn great attention due to their higher performances. The improved performances possibly attributed to the more accessible active sites, exposure of numerous defects and exchangeable coordination positions (Dhakshinamoorthy et al., 2019). For instance, Dong et al. developed planar porous carbon nanosheets by means of layered-nanospace-confinement strategy. The 2D nanostructure provided larger exposed active surface area, more accessible and higher porosity and faster diffusion kinetics, making the material with superior activity for oxygen reduction reactions (Dong et al., 2017). Nevertheless, most of the researches concentrated on the fields of electrochemistry and energy storage, such as supercapacitor and electrocatalysis (Jiang et al., 2017; Huang et al., 2017), while were rarely seen in adsorption, especially in liquid-phase adsorption. Therefore, it might be worth trying and exploring the performances of two-dimension carbonaceous materials in liquid-phase adsorption reaction.

Herein, we selected Zn-ZIF-L as a precursor for its two-dimension leaf-like morphology and considerable nitrogen content. With the assistance of etching agents (KCl) that could attenuate the effect of sintering and aggregation, Zn-ZIF-L was exfoliated into sheets by two-step pyrolysis in N_2 atmosphere. The obtained nanoporous carbon possessed the superiority of 2D materials with more accessible adsorptive sites. Besides, the dopant of N atoms in the carbon framework helped to promote the surface activity. The combination of the above advantages would make it a satisfactory adsorbent for TC removal in aqueous solutions. In addition, pyrolysis temperature had a great impact on the products and was investigated further at a series of temperature (600–900 °C). The adsorption kinetics and isotherms were studied systematically along with adsorption thermodynamics. Furthermore, we explored the performances of adsorbents, including influence factors (pH, ionic strength and HA) and recyclability. More importantly, RSM was applied to analyze the interactions between each two factors and optimize experimental condition. In a word, we expected this work could bring something useful and significative for other researches.

2. Experiment

2.1. Chemicals

Chemicals used throughout the experiment were as followed: zinc nitrate hexahydrate ($Zn(NO_3)_2{\cdot}6H_2O$, 99 %), 2-methylimidazole (MIM, 98 %), potassium chloride (KCl, 99.5 %), tetracycline (TC, 99.7 %), ethanol (99.7 %) and concentrated sulfuric acid (98 %). All of the purchased chemical medicines were used with no purification. Furthermore, ultrapure water (18.25 MΩ cm) was utilized as solvents during the experiment.

2.2. Synthesis of Zn-ZIF-L and NC-X (X = 600, 700, 800)

Zn-ZIF-L was prepared by stirring at room temperature according to the previously reported methods (Chen et al., 2013). Briefly, MIM (0.595 g) and $Zn(NO_3)_2{\cdot}6H_2O$ (1.313 g) were dissolved in 40 mL ultrapure water, respectively. After a quick mixing, the mixed solution was stirred and lasted 4 h on low speed. The obtained white precipitates were centrifuged and washed by ultrapure water. Ultimately, the products (Zn-ZIF-L) were obtained by vacuum drying at 60 °C for 10 h.

Secondly, Mix Zn-ZIF-L (about 500 mg) with potassium chloride solution by stirring. Subsequently, the solution got dried in a vacuum drying oven at 60 °C. The obtained solid mixtures were grinded and pyrolyzed in a tube furnace under the protection of nitrogen. Before the beginning of carbonization, the tube furnace was fed with nitrogen flow for 1 h to remove air (oxygen) inside. The heating rate was 5 °C min^{-1} during the whole pyrolysis process. When the temperature reached to 400 °C, the state was kept for 2 h. After that, as the temperature rose to the final pyrolysis temperature (600, 700, 800 °C), the state was maintained for another 2 h. At last, the products were washed by 0.5 mol L^{-1} H_2SO_4 and ultrapure water followed by vacuum drying, and were marked as NC-X (X = 600, 700, 800).

2.3. Characterization of NC-X (X = 600, 700, 800)

The morphological structures of NC-X were analyzed via scanning electron microscopy (SEM, Quanta 250 FEG). The X-ray diffraction (XRD) patterns were acquired through X-ray diffractometer (Bruker D8 Advance) with a range of 5° - 90°. The elementary composition was detected by X-ray photoelectron spectrums (XPS, EscaLab Xi+). Raman spectra (RS) was obtained from the Raman spectrophotometer (Horiba

Scientific LabRAM HR Evolution) as the wave numbers ranged from 800 to 2000 cm^{-1}. Fourier transform infrared (FT-IR) spectra was investigated by FT-IR spectrophotometer (Bruker Vertex 70). Depending on the nitrogen adsorption-desorption process, pore size distribution and surface area of the materials were studied via Brunauer-Emmett-Teller (BET) analytical instrument (Maike ASAP 3460). Also, zeta potentials of adsorbents were measured in aqueous solutions and TC solutions at different pH values by Zeta-sizer Nano-ZS (Malvern, UK).

2.4. Adsorption experiments

The stock TC solution of 100 mg L^{-1} was prepared by dissolving TC into ultrapure water. After diluting the stock solution (100 mg L^{-1}), a series of low concentration solutions (10–80 mg L^{-1}) were obtained. Adsorption experiments were conducted in conical flasks with TC solution (50 mL, 10–100 mg L^{-1}) and 10 mg adsorbent. To reach the adsorption equilibrium, the conical flasks were shaken in a thermostatic shaker for 60 min with the fixed temperature at the speed of 160 rpm. Subsequently, the suspension solutions were filtered by PVDF (polyvinylidene fluoride) filters (0.45 μm), and concentration of the final solution was measured by UV spectrophotometer, assisted with Liquid Chromatogram.

Single influence factors, including pH (2–12), HA and ionic strength (Na^+, Ca^{2+}), were considered. Adsorption kinetic was studied by a series of TC solutions (10–100 mg L^{-1}). Adsorption thermodynamics experiments were conducted at different temperatures (298, 308, 318 K). More detailed information about kinetics, isotherms, thermodynamics, and so on, were showed in Table S1.

2.5. RSM design model: Central composite design (CCD)

Based on the analysis of single influence factors, to discuss interactions among the single factors and evaluate the factors which had a primary effect on adsorption capacity, central composite design (CCD) was chosen to analyze adsorption process and optimize existing experiment conditions. In this design, four independent factors, including pH (x_1), ionic strength of Ca^{2+} (x_2), HA (x_3) and concentration of TC (x_4) were selected as experimental variables. Each of them was set with five levels (-2, -1, 0, 1, 2). The response variable (y) represented the adsorption quantity of TC. On the basis of second-order response models, the relationship between the response variable (y) and variables (x_1, x_2, x_3, x_4) was fitted with a quadratic multinomial equation (Asfaram et al., 2015; Song et al., 2014):

$$y = \beta_0 + \sum_{i=1}^{4} \beta_i x_i + \sum_{i<j}^{4} \beta_{ij} x_i x_j + \sum_{i=1}^{4} \beta_{ii} x_i^2 \quad (1)$$

where y represented adsorption quantity of TC, β_0 β_0 was the model constant parameter, x_i x_i represented four variables (pH, ionic strength of Ca^{2+}, HA, concentration of TC), β_i β_i represented the linear coefficient, β_{ij} β_{ij} represented the interaction coefficient, β_{ii} β_{ii} represented the quadratic coefficient. Besides, four experimental variables and response variable were listed in Table 1.

Table 1
Experimental variables of central composite design.

Factors	Levels				
	Low (-1)	Central (0)	High (1)	-α	+α
X_1: pH	5	7	9	3	11
X_2: ionic strength of Ca^{2+} (mol L^{-1})	0.10	0.15	0.20	0.05	0.25
X_3: HA (mg L^{-1})	20	30	40	10	50
X_4: concentration of TC (mg L^{-1})	40	60	80	20	100

3. Results and discussion

3.1. Characterizations of Zn-ZIF-L and NC-X (X = 600, 700, 800)

The morphology of the synthesized materials was characterized via SEM characterization. As showed by Fig. 1a, the as-prepared Zn-ZIF-L presented leaf-like morphology and its size was about 2 μm × 5 μm with a thin thickness (approximately 100 nm), which was similar with the reported literature (Chen et al., 2013). Currently, direct carbonization of Zn-ZIF-L in a N_2 flow led to sintering and aggregation compared with the original leaf-like shape (Fig. S1), which might result from the lower morphology stability of Zn-ZIF-L (Zhong et al., 2014a). When KCl was added into Zn-ZIF-L precursors, the products were exfoliated into sheets in the pyrolysis process. As shown in Fig. 1b–d, when pyrolysis temperature rose from 600 °C to 800 °C, morphology of NC-X transformed into sheets gradually. During the process of thermal exfoliation, the etching agent (KCl) might react with carbon from Zn-ZIF-L following the formula (Xia et al., 2019): $2KCl + 3H_2O + C \rightarrow K_2CO_3 + 2HCl + 2H_2$. It could be inferred that the process was an endothermic reaction referring to the effect of thermal exfoliation. Therefore, the higher temperature helped to facilitate the thermal exfoliation.

The XRD pattern of Zn-ZIF-L was coincidental with the simulation of Zn-ZIF-L (Fig. 2a), demonstrating that the Zn-ZIF-L was synthesized successfully. It was obvious that the lattice structures of NC-X (X = 600, 700, 800) were distinct from Zn-ZIF-L (Fig. 2). According to the analysis of XRD pattern (Fig. 2b), there were two distinguishable diffraction peaks. A peak located at about 25° and another peak was at about 44°, which were derived from (002) and (101) planes of graphitic carbon, respectively (Li et al., 2017). The peak intensities of the three samples with different carbonization temperatures were nearly at the same levels, suggesting that the crystalline phase of NC-X had no obvious change at higher carbonization temperature.

The surface element state of Zn-ZIF-L and NC-800 were studied by XPS. As showed in Fig. 3 and Table S2, Zn-ZIF-L and NC-800 mainly consisted of four elements containing C, N, O and Zn. After carbonization at high temperature, the content of Zn element greatly reduced from 8.93 % to 1.13 %, leaving a small quantity wrapped by the carbon layers. A part of Zn evaporated during the carbonization process and the rest were washed by dilute H_2SO_4 solutions. Besides, the total N content decreased with temperature increasing (Table S6), which might be caused by the higher degree of thermal exfoliation and damage of carbon structure (Tang et al., 2015). For the C 1s spectrum (Fig. 3b), there were four peaks corresponded to C=C (284.7 eV), C–C (285.7 eV), C–N (286.3 eV) and O–C=O (289.0 eV), respectively (Xu et al., 2019b). Usually, N atoms would form various bonds with C atoms in the pyrolysis process. The N 1s spectra could be separated and fitted into four peaks (Fig. 3c), which represented pyridinic N (398.4 eV), pyrrolic N (400.1 eV), graphitic N (401.3 eV) and N–O species (403.4 eV) (Zhong et al., 2014b; Wang et al., 2019). The relative contents of each nitrogen configuration in NC-800 were 53.69 %, 22.59 %, 21.79 % and 1.93 %, respectively. Except for graphitic N, the rest formed at the edge of carbon frameworks might lead to more defects and provide more adsorption sites for TC molecules (Li et al., 2017). In short, the conclusion from XPS proved the effective doping of nitrogen into carbon structures in NC-800.

For further investigation of NC-X (X = 600, 700, 800), Raman spectra was used to identify the degree of graphitization in carbonaceous materials, which could be calculated by the intensity ratios between D band (~ 1340 cm^{-1}) and G band (~ 1580 cm^{-1}) (Ye et al., 2017). According to Raman spectra pattern (Fig. 4a), the intensity ratios (I_D/I_G) of NC-X (X = 600, 700, 800) were 0.99, 1.05 and 1.10, respectively. The higher intensity ratio corresponding to the lower degree of graphitization signified more defects with higher porosity. Generally, more defects could supply more adsorption sites (Li et al., 2017), which was in favor of the adsorption reaction. Hence, the Raman

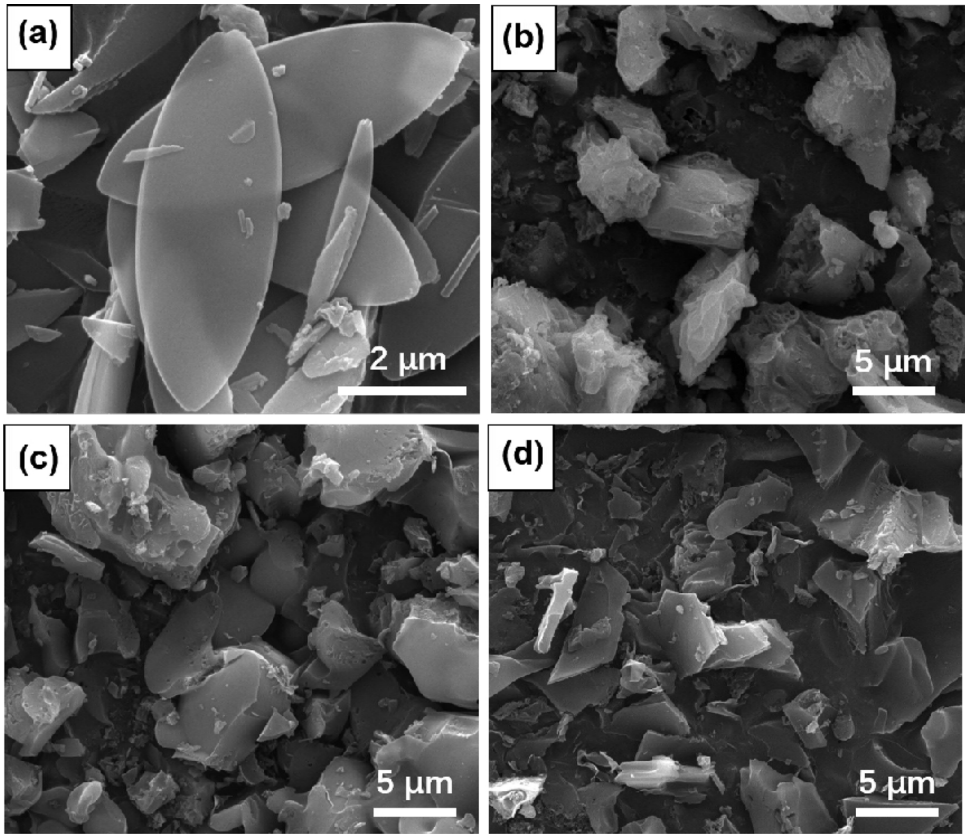

Fig. 1. SEM images of (a) Zn-ZIF-L, (b) NC -600, (c) NC-700, (d) NC-800.

analysis indicated that higher carbonization temperature promoted the thermal exfoliation and formed more defects at the edge of carbon frameworks.

To obtain the information about functional groups, the FT-IR spectroscopy of Zn-ZIF-L and NC-800 were acquired and showed in Fig. 4b. As for Zn-ZIF-L, the peak located in 421 cm^{-1} belonged to Zn-N. The broad band at around 3400 cm^{-1} derived from N–H group in dimethylimidazole and O–H in water adsorbed from the air, while the bands occurred at 1584 cm^{-1} was the stretch of C=N groups. Otherwise, the bands between 600 cm^{-1} and 1500 cm^{-1} resulting from the stretching and bending of dimethylimidazole ring (Low et al., 2014; Nasir et al., 2018). The data analysis proved the successful preparation of Zn-ZIF-L and was in accordance with the result of XRD. By contrast, only a few bands left after the carbonization. The peak at 1584 cm^{-1} was caused by the stretching of C=N and the bands at around 1200 and 3400 cm^{-1} belonged to the stretching form N–H groups (Zheng et al., 2014). The existent C=N and N–H testified to the successful doping of nitrogen in NC-800.

The types of N_2 adsorption-desorption curves were measured by BET analysis. As illustrated in Fig. 5a, differing from the Zn-ZIF-L conforming to the type I isotherm, the NC-X (X = 600, 700, 800) belonged to the type IV isotherm with a type H4 hysteresis loop. The fast adsorption of N_2 at low pressure ($P/P_0 < 0.05$) indicated that a large number of micropores or mesopores existed in NC-X. By the way, based on the pore diameter distribution, micropores and mesopores (< 5 nm) were predominant in NC-X (Fig. 5b), which were more than in Zn-ZIF-L. As observed in Table 2, the surface area and total pore volume of NC-X increased greatly in comparison to Zn-ZIF-L precursor. The NC-800 had the maximal surface area (2195.57 $m^2\ g^{-1}$) and porosity (1.34 $cm^3\ g^{-1}$), making it more beneficial for adsorption process.

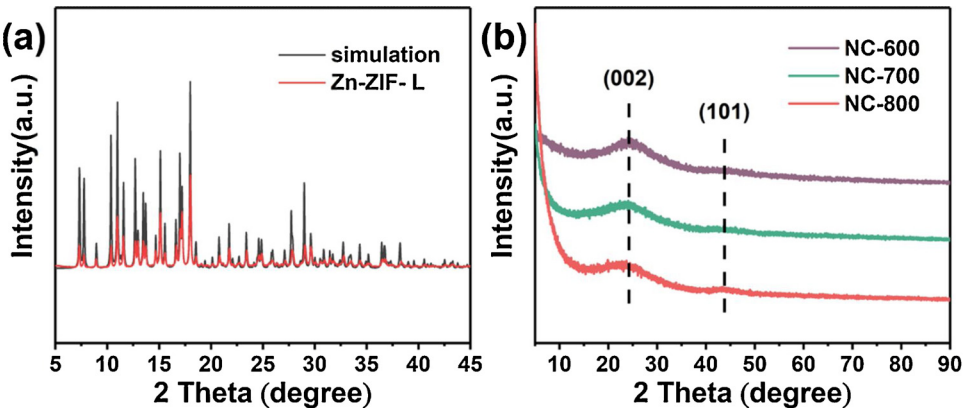

Fig. 2. The XRD patterns of (a) Zn-ZIF-L, (b) NC-X (X = 600, 700, 800).

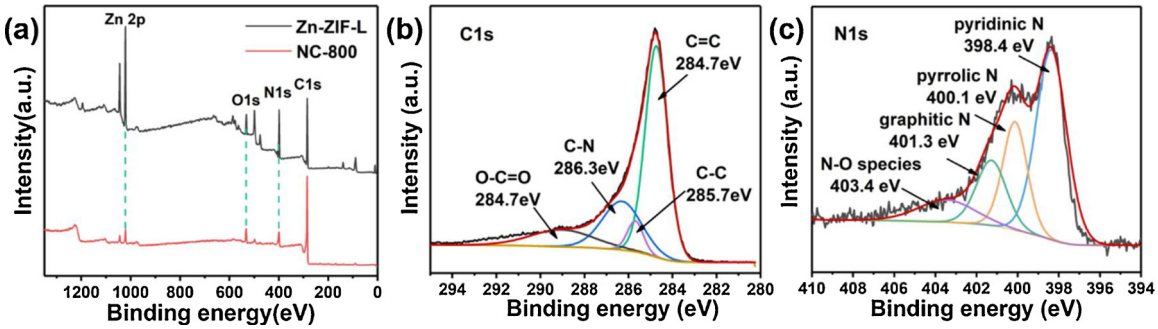

Fig. 3. XPS spectra of NC-800 and Zn-ZIF-L: (a) survey, (b) C 1s and (c) N 1s of NC-800.

3.2. The performances of adsorption studies

To acquire the best adsorption capacities of adsorbents, the carbonization of Zn-ZIF-L mixed with KCl was carried out at different temperature (600, 700, 800, 900 °C). As observed from Fig. S2, with the temperature rising (600–800 °C), the adsorptive capacities of NC-800 showed an increasing trend relevant to the higher degree of thermal exfoliation, larger surface area and higher porosity. The removal efficiency of TC improved greatly from 7.26 % to 99.82 %. However, when the temperature reached 900 °C, the adsorption performance of NC-900 declined to 91.23 % as well as the reduced porosity and specific surface area. Since the melting point of KCl was 770 °C, more evaporation loss of KCl might inhibit the reaction ($2KCl + 3H_2O + C \rightarrow K_2CO_3 + 2HCl + 2H_2$) and reduced the effect of thermal exfoliation, leading to low adsorption ability. In consideration of the adsorption capacities and energy consumption intensity, NC-800 was chosen as adsorbents in following experiments.

3.2.1. Adsorption kinetics and adsorption isotherms studies

The adsorption kinetics and isotherms of NC-800 were investigated to better make sense of adsorption process with different initial contact time. For adsorption kinetics, pseudo-first-order and pseudo-second-order models were utilized to match with adsorption data. Based on Fig. 6a and b, the pseudo-second-order model fitted perfectly with data points and was more preferable than the pseudo-first-order model. Also, the correlation coefficients of pseudo-second-order model (R^2 = 0.99988) was much higher than another model (R^2 = 0.87901), revealing that it could describe the adsorptive behavior better. Therefore, the above results suggested that chemisorption might play a dominant role in adsorption reactions (Xiong et al., 2019a). Moreover, intra-particle diffusion model was utilized to explain the diffusion behavior during adsorptive reaction. The fitting region was divided into two portions (Fig. 6c). The first portion fitted to the line with a steep slope represented a fast adsorption process, since the two-dimension structure of NC-800 made it more accessible for the transfer and diffusion of TC molecules onto adsorbents. The second portion with a gradual slope meant slow adsorption equilibrium over time (Yang et al., 2019). However, the fitted lines did not go through the origin, revealing that the rate-limiting step was not dominated by intra-particle diffusion (Xiong et al., 2018).

Three models (Langmuir, Freundlich and Temkin) were employed to fit experiment data, so that we could further investigate adsorption type of NC-800. From the results of Fig. 6e and f and Table 3, Langmuir model was in accordance with the adsorption data better. At the same time, compared with the Freundlich model (R^2 = 0.99093) and Temkin model (R^2 = 0.96680), Langmuir model had the highest correlation coefficient (R^2 = 0.99899). Notably, it confirmed that the adsorption behaviors occurred in adsorbents could be monolayer adsorption (Li et al., 2018). In addition, the maximal adsorptive capacity estimated by Langmuir model was 350.88 mg g^{-1} that approached to experimental value (347.06 mg g^{-1}) and better than some adsorbents listed in Table S3.

3.2.2. Adsorption thermodynamic studies

Thermodynamic experiments were carried out with various temperatures (298, 308, 318 K). It was evident that adsorption capacities increased as temperature rising (Fig. S3a), indicating the adsorption process belonged to an endothermic reaction. For further understanding of the thermodynamic process, several parameters were calculated in the following formulas (Liu, 2009):

$$ln(\frac{q_e}{C_e}) = -\frac{\Delta H}{RT} + \frac{\Delta S}{R} \quad (2)$$

$$\Delta G = \Delta H - T\Delta S \quad (3)$$

Above formulas, R (8.314 J mol^{-1} K^{-1}) was the gas constant; ΔG was Gibbs free energy; ΔH was enthalpy; ΔS was entropy; T represented thermodynamic temperature.

According to Table 4, with rising temperature, the diminution of ΔG

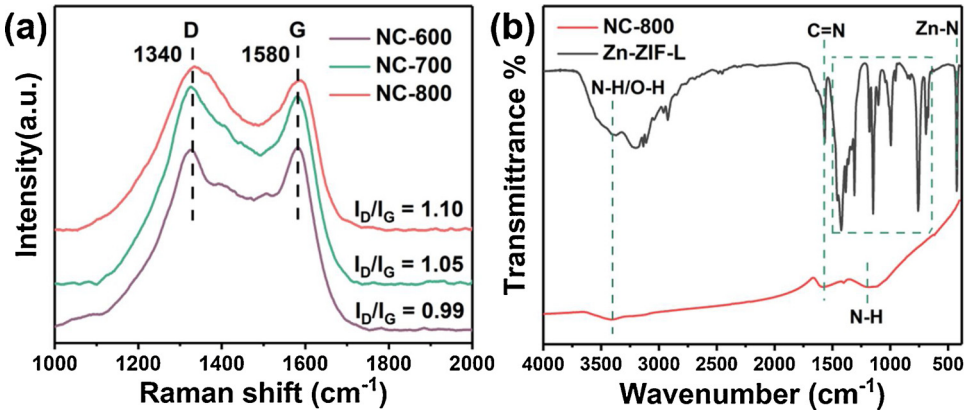

Fig. 4. Raman spectra of NC-X (a) and FT-IR spectra of Zn-ZIF-L and NC-800 (b).

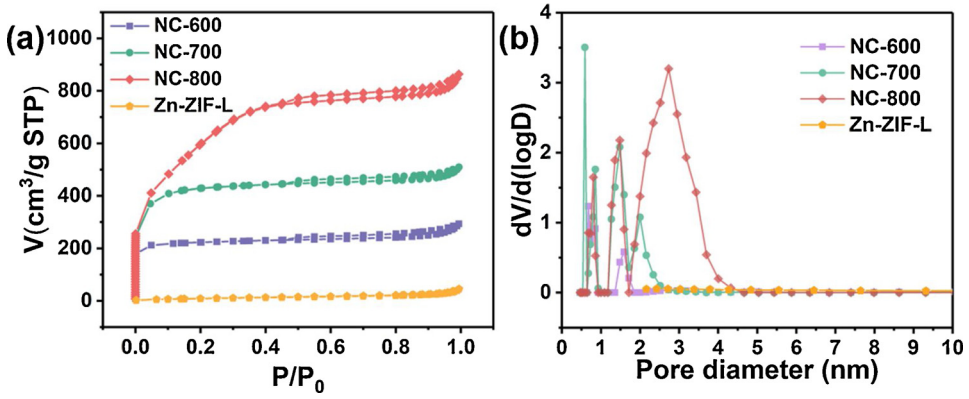

Fig. 5. N_2 adsorption-desorption isotherms (a), pore diameter distribution obtained by DFT model (b) of NC-X (X = 600, 700, 800) and Zn-ZIF-L.

Table 2
Surface area, pore size and pore volume parameters of NC-X.

Materials	NC-600	NC-700	NC-800	NC-900	Zn-ZIF-L
Surface area[a] ($m^2\ g^{-1}$)	644.12	1261.31	2195.57	1644.47	36.25
Pore size[b] (nm)	6.31	4.88	2.67	3.56	6.57
V_t[c] ($cm^3\ g^{-1}$)	0.46	0.79	1.34	1.15	0.07

[a] Measured by N_2 adsorption with the Brunauer-Emmett-Teller (BET) method.
[b] Pore size in diameter calculated by the desorption data using Barrett-Joyner-Halenda (BJH) method.
[c] Total pore volume determined at P/P_0 = 0.99.

Table 3
The parameters of Langmuir, Freundlich and Temkin isotherms models.

Langmuir			Freundlich			Temkin	
q_m	K_L	R^2	1/n	K_F	R^2	K_T	R^2
350.88	2.036	0.99899	0.153	214.272	0.99093	30.939	0.9668

Table 4
The thermodynamic parameters for TC adsorption.

T (K)	ΔG (KJ mol^{-1})	ΔS (KJ $mol^{-1}\ K^{-1}$)	ΔH (KJ mol^{-1})
298	−9.32		
308	−10.26	0.09	18.39
318	−11.18		

ranging from −9.32 to −11.18 KJ mol^{-1} manifested TC adsorption belonged to spontaneous process and was easier to happen at the higher temperature. ΔH with a positive value (18.39 KJ mol^{-1}) proved the adsorption of TC molecules was endothermal, which was in line with the analysis about experiment data. Besides, the degree of disorder increased at the adsorbent-adsorbate interface on account of ΔS greater than zero (Yu et al., 2019).

3.2.3. Effect of pH

Solution pH value played a significant part in adsorptive reaction via protonation and deprotonation of TC molecules (Bhadra et al., 2018). As presented in Fig. 7a, it was clear that the adsorption capacity maintained relatively high level except that pH value was 12. Nevertheless, pH value of 8 became a turning point and the adsorption ability decreased after that. Moreover, TC was an amphoteric compound with three dissociation constants (pK_a : 3.32, 7.78 and 9.58), indicating TC could transform into several forms: positive ions (TC^+, pH < 3.32),

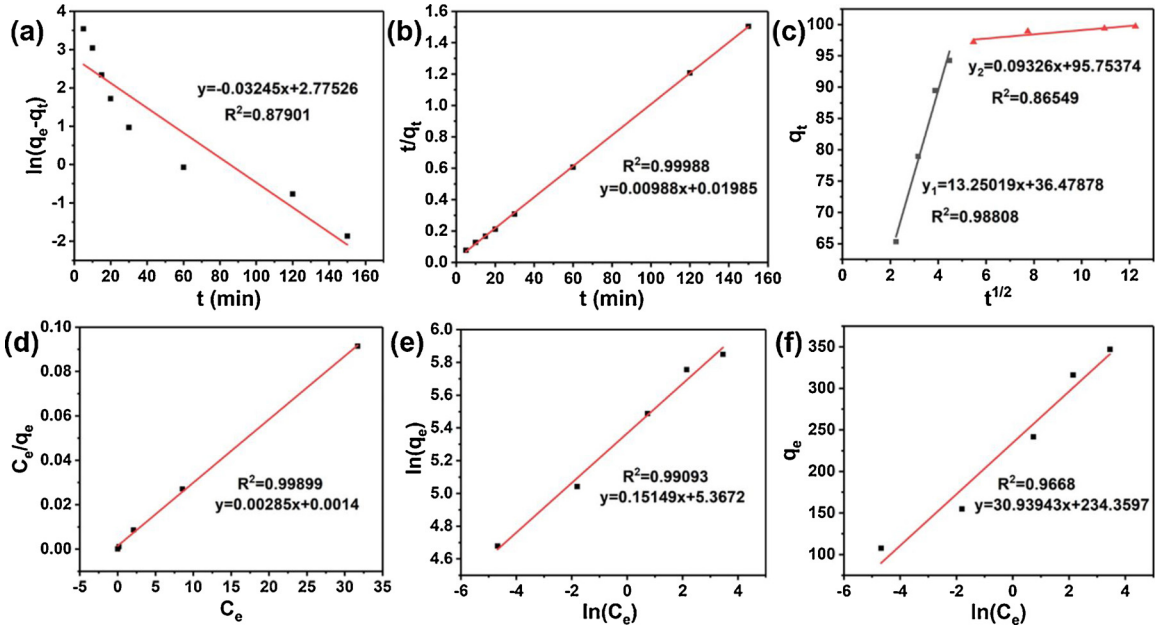

Fig. 6. The pseudo-first-order (a), pseudo-second-order (b), intra-particle diffusion model (c), Langmuir (d), Freundlich (e) and Temkin isotherms models (f) of NC-800. (Experiment conditions: adsorbent dosage = 0.2 g L^{-1}, T = 298 K, pH = 4.50).

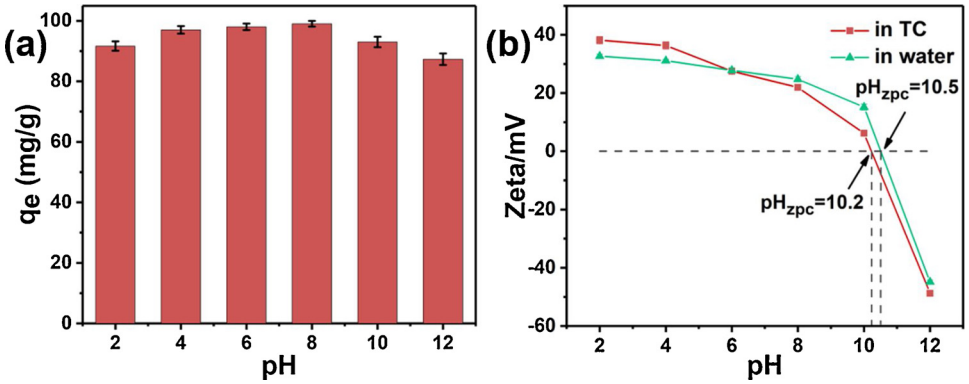

Fig. 7. Effect of solution pH on the adsorption of TC (a) and Zeta potential of NC-800 in different solutions (b). (Experiment conditions: initial TC concentration = 20 mg L^{-1}; adsorbent dosage = 0.2 g L^{-1}, T = 298 K).

neutral molecule (TC, 3.32 < pH < 7.78) and negative ions (TC^-, 7.78 < pH < 9.58; TC^{2-}, pH < 9.58) (Jin et al., 2019). Zero potential point corresponded to the pH at which the surface of material appeared neutral with zeta potential of zero (Sarker et al., 2017b). The zero potential point obtained from TC solution (approximately 10.2) made it clear that the adsorbents were positively charged when pH value was less than 10.2. Besides, the left shift of zero potential point in TC solution was caused by the adsorption of TC, resulting in the change of surface charge. Therefore, the electrostatic attraction between NC-800 and TC might be the main reason for high adsorption ability at pH around 8. Meanwhile, H-banding interaction among polar groups including N–H (pyridinic N, pyrrolic N) in NC-800 and O–H (hydroxy, carbonyl) in TC molecules contributed to excellent adsorptive property at pH 2–6 (An et al., 2018). Besides, π-π interactions between benzene ring in TC and sp^2 graphitic carbon planes in NC-800 also made a contribution (Gao et al., 2012). On the contrary, as pH reached 12, strong electrostatic repulsive-force led to low adsorption. In conclusion, electrostatic interaction and H-banding interaction had an important influence on adsorption process.

3.2.4. Effect of ionic strength and humic acid

In fact, the compositions of actual wastewater were complex, since a large number of compounds existed in it, such as saline ions (Na^+, Ca^{2+}) and HA. To explore the effects of Na^+, Ca^{2+} and HA, a sequence of tests were conducted and the results were exhibited in Fig. 8. In terms of ionic strength (Fig. 8a), there was not much change as the concentrations of NaCl or $CaCl_2$ increased. It was distinct that NC-800 had better antijamming capability for saline ions in solution. This might be due to electrostatic interactions from NC-800 and NaCl (or $CaCl_2$) (Xiong et al., 2019b). In this experimental condition (pH was around 4.50), NC-800 was positively charged and generated repulsive force with Na^+ or Ca^{2+}. Simultaneously, this phenomenon resulted in low-level competition with TC molecules for active adsorption sites.

With regard to the effect of HA, Fig. 8b revealed that HA inhibited the adsorption of TC as adding more HA into solution. Firstly, the zero potential point of HA was around pH 2.0 and HA was negatively charged throughout the experiment. Hence, HA could be adsorbed by NC-800 (positively charged) via electrostatic interaction, causing the reduction of adsorption sites (Yang et al., 2011). On the other hand, HA molecules were large and complicated with abundant functional groups. They might react with TC molecules and produce complex surface complexation, which went against the adsorption of TC. In brief, the above reasons brought about the relative low adsorption ability.

3.3. Experimental results of central composite design

3.3.1. Model fitting and analysis of variance

In consideration of complexity about actual water, four single influence factors were chosen as experiment variables and already listed in Table 1. Also, the response variable (q_e) and 30 groups of parallel experiments were showed in Table S4.

Referring to ANOVA (analysis of variance) in Table S5, the F-value (32.41) and P-value (< 0.0001) indicated this model was significant. The value of R-squared reached 0.9680. Meanwhile, the adeq precision was 21.821 (< 4). Both of them revealed the better goodness of fitting and predictability about the model. In this model, a quadratic polynomial equation was acquired by data processing:

$$y = -215.51 + 41.14X_1 + 11.58X_2 + 2.87X_3 + 8.85X_4 - 39.72X_1X_2 + 0.0123X_1X_3 - 0.526X_1X_4 - 4.56X_2X_3 + 2.32X_2X_4 - 0.00477X_3X_4 - 1.52X_1^2 + 531.63X_2^2 - 0.0287X_3^2 - 0.0273X_4^2$$

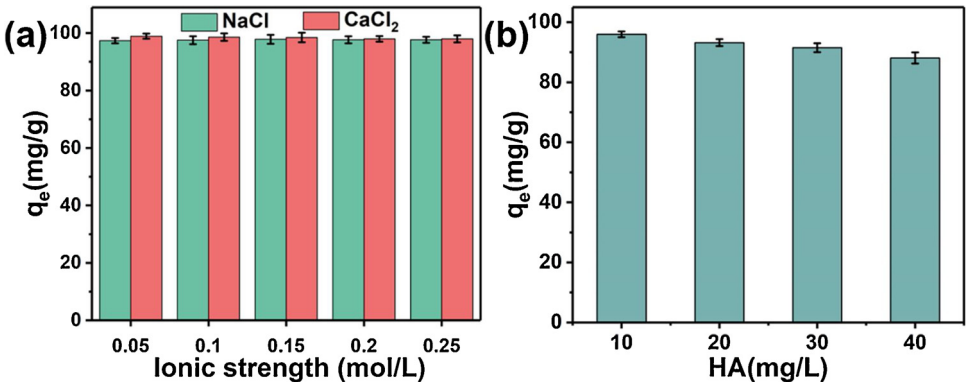

Fig. 8. Effect of ionic strength (a) and HA (b) on the adsorption of TC onto NC-800. (Experiment conditions: initial TC concentration = 20 mg L^{-1}; adsorbent dosage = 0.2 g L^{-1}, T = 298 K, pH = 4.50).

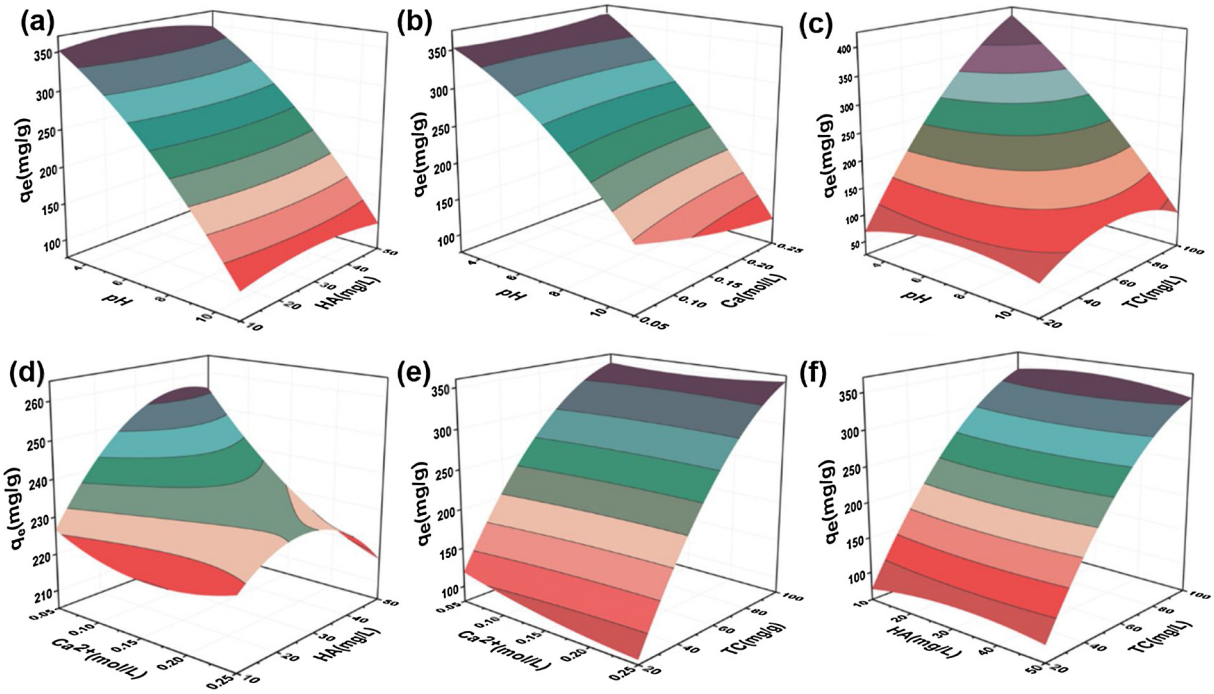

Fig. 9. Response surfaces for TC removal: (a) pH-HA, (b) pH-Ca^{2+}, (c) pH-TC, (d) Ca^{2+}-HA, (e) Ca^{2+}-TC and (f) HA-TC.

$$y = -215.51 + 41.14X_1 + 11.58X_2 + 2.87X_3 + 8.85X_4 - 39.72X_1X_2 + 0.0123X_1X_3 - 0.526X_1X_4 - 4.56X_2X_3 + 2.32X_2X_4 - 0.00477X_3X_4 - 1.52X_1^2 + 531.63X_2^2 - 0.0287X_3^2 - 0.0273X_4^2 \quad (4)$$

Moreover, P-value (< 0.05) represented significant model terms, including X_1, X_4, X_1X_4, $X_1{}^2$ and $X_4{}^2$. While others (X_2, X_3, X_1X_2, X_1X_3, X_2X_3, X_2X_4, X_3X_4, $X_2{}^2$, $X_3{}^2$) were not significant in this model. According to the F-value, the influences of each factor were followed the order: TC > pH > Ca^{2+} > HA. For best adsorption capacity, optimal experiment condition was obtained via model prediction: TC 100 mg L^{-1}, Ca^{2+} 0.25 mol L^{-1}, HA 20 mg L^{-1}, pH 3, under which the predicted value of adsorption could be 427.41 mg L^{-1}.

3.3.2. Analysis of response surface plots

The interactions and relationships among the four variables were investigated and presented in Fig. 9. Each pattern was drawn by two variables with another two fixed parameters. Form Fig. 9c, the tendency of pH at low concentration of TC showed a similar result when we only considered the effect of pH. Nevertheless, the diminishment of adsorption quantity could be clearly observed at high concentration. It revealed that electrostatic interaction might no longer be predominant in adsorption process. Instead, the hydrogen bond might be dominant in high concentration of TC, and more hydrogen bond was likely to form with higher density of TC molecules in solution (Ahmed and Jhung, 2017). In addition, the increase of pH value caused the deprotonation of TC molecules and NC-800, which was unfavorable for the formation of hydrogen bond. This result led to the reduction of adsorption capacity directly. Usually, high concentration promoted the adsorption resulting from a high concentration gradient driving force (Wang et al., 2016). When pH value was fixed (3–11), the change of adsorption capacity caused by HA or Ca^{2+} was in agreement with the previous analysis considering the effect of HA or Ca^{2+} only (Fig. 9a and b). Fig. 9e and f presented a similar tendency with the increase of TC concentration; meanwhile the behavior of HA or Ca^{2+} had no distinct difference with the results of Fig. 9a and b. As for Fig. 9d, adsorption of TC molecules increased with the addition of HA. A possible reason could be that the HA molecules adsorbed by NC-800 might combine with TC molecules at high concentration of TC by means of surface complexation, indirectly enhancing adsorption ability. Otherwise, high concentration of Ca^{2+} inhibited the adsorption process. This phenomenon probably was caused by the existence of adsorbed HA that intensified the competition for adsorptive sites between Ca^{2+} and TC molecules at high TC concentration.

3.4. Possible adsorption mechanisms for TC

To figure out the adsorptive behaviors occurred in adsorption process, some possible adsorption mechanisms were proposed (Fig. 10). Generally, adsorption principles of TC molecules could be divided into two parts, including physisorption and chemisorption. The huge specific surface area and high porosity of NC-800 created better conditions for pore/size-selective adsorption. Hence, it could accelerate the diffusion and adsorption of TC molecules, which was in favor of adsorptive reaction. Moreover, electrostatic interaction made a significant contribution to adsorption mechanisms. The deprotonation and protonation of adsorbents and adsorbates would alter their surface charge. It resulted in electrostatic attraction or repulsion among them and directly affected the adsorption capacity. Hence, the interpretations about the effect of pH and Ca^{2+} attributed to electrostatic interaction. Meanwhile, in this study, hydrogen bond was another crucial portion to explain the adsorption principles. The hydrogen bond between TC molecules (hydroxy, carbonyl) and NC-800 (pyridine N, pyrrole N) combined them together, which was benefit for the adsorption of TC onto NC-800. Otherwise, the π-π interaction could be taken into consideration. It was ascribed to the interactions caused by benzene ring in TC and sp^2 graphitic carbon planes in NC-800. Therefore, the adsorption process was complicated, which combined chemical and physical interactions.

3.5. Recyclability tests

Recyclability of the adsorbent occupied great importance in practical application. To estimate the performance of NC-800, several cyclic adsorption experiments were conducted. In the process of desorption, the adsorbents were soaked in ethanol and shook for 4 h. As shown in Fig. 11, with the increase of cycle numbers, there was no apparent

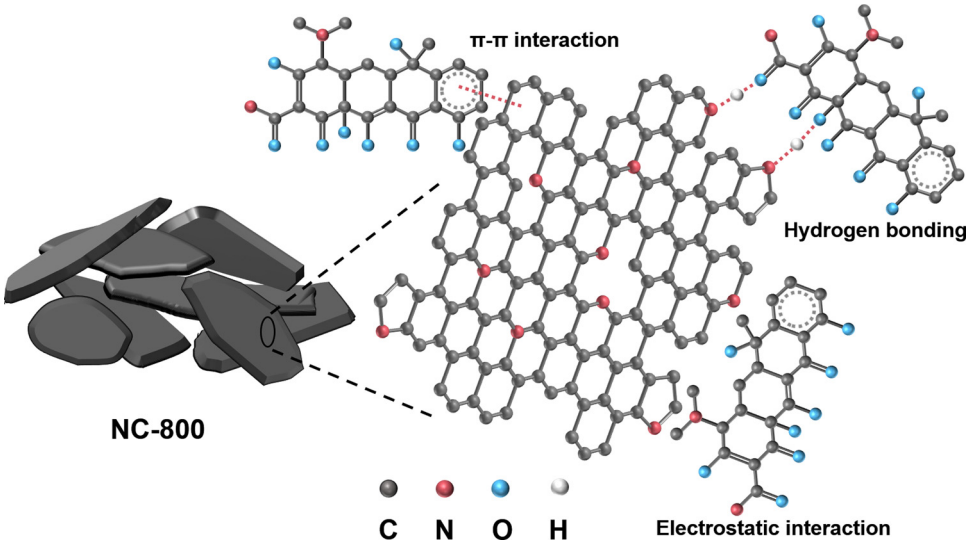

Fig. 10. Proposed adsorption mechanisms of TC on NC-800.

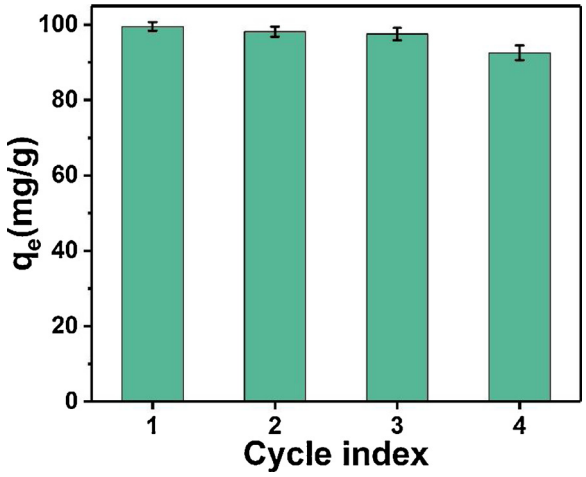

Fig. 11. Cycle index of NC-800. (Experiment conditions: initial TC concentration =20 mg L^{-1}; adsorbent dosage =0.2 g L^{-1}, T =298 K, pH = 4.50).

decrease in the adsorption ability of NC-800, which indicated the great reusability of NC-800. However, to reach the adsorption equilibrium, adsorption time multiplied as cycle numbers increased (Fig. S4). It revealed that the TC molecules could not be removed completely in the desorption process. The residual TC molecules occupied the active sites and blocked the pore structures, leading to low rate of adsorption. Overall, NC-800 exhibited the excellent recyclability and was supposed to be a potential adsorbent to remove TC in aqueous solutions.

4. Conclusion

In this study, two-dimension NC-800 was synthesized successfully by two-step carbonization and thermal exfoliation of Zn-ZIF-L in a nitrogen atmosphere. The NC-800 with unique sheet structure and abundant N-doping amount exhibited quick and effective adsorption for TC at a wide pH range (2–10) coupled with good antijamming capability for Na^+ and Ca^{2+} ions. The adsorption behaviors of NC-800 matched better with pseudo-second-order kinetic and Langmuir isothermal models, revealing chemical and monolayer adsorption for TC molecules. Also, TC adsorption was a spontaneous and endothermic process according to thermodynamic data. Moreover, except for ionic strength (Na^+ and Ca^{2+}), pH and HA had an obvious effect on adsorption reaction and the possible mechanisms could be expounded by electrostatic interaction, hydrogen bond interaction and surface complexation. Meanwhile, other adsorption principles, such as π-π interaction and pore/size-selective effect, were considered as well. Besides, RSM was utilized to investigate the interactions among variables and optimize experimental condition. In summary, NC-800 with high adsorption capacity of TC and great recyclability might become a potential adsorbent in wastewater treatment for TC antibiotic removal.

CRediT authorship contribution statement

Haihao Peng: Data curation, Writing - original draft. **Jiao Cao:** Writing - review & editing. **Weiping Xiong:** Supervision, Writing - review & editing. **Zhaohui Yang:** Supervision, Funding acquisition. **Meiying Jia:** Writing - review & editing. **Saiwu Sun:** Writing - review & editing. **Zhengyong Xu:** Writing - review & editing. **Yanru Zhang:** Writing - review & editing. **Hongchun Cai:** Writing - review & editing.

Declaration of Competing Interest

The authors declare that they have no known competing financial interests or personal relationships that could have appeared to influence the work reported in this paper.

Acknowledgements

The study was financially supported by the National Natural Science Foundation of China (51878258, 51521006).

Appendix A. Supplementary data

Supplementary material related to this article can be found, in the online version, at doi:https://doi.org/10.1016/j.jhazmat.2020.123498.

References

Ahmed, I., Jhung, S.H., 2017. Applications of metal-organic frameworks in adsorption/separation processes via hydrogen bonding interactions. Chem. Eng. J. 310, 197–215.
An, H.J., Bhadra, B.N., Khan, N.A., Jhung, S.H., 2018. Adsorptive removal of wide range of pharmaceutical and personal care products from water by using metal azolate framework-6-derived porous carbon. Chem. Eng. J. 343, 447–454.
Asfaram, A., Ghaedi, M., Agarwal, S., Tyagi, I., Kumar Gupta, V., 2015. Removal of basic dye Auramine-O by ZnS:Cu nanoparticles loaded on activated carbon: optimization of parameters using response surface methodology with central composite design. RSC Adv. 5, 18438–18450.
Bai, Y., Xu, R., Wang, Q.P., Zhang, Y.R., Yang, Z.H., 2019. Sludge anaerobic digestion with high concentrations of tetracyclines and sulfonamides: dynamics of microbial

communities and change of antibiotic resistance genes. Bioresour. Technol. 276, 51–59.
Bhadra, B.N., Vinu, A., Serre, C., Jhung, S.H., 2019. MOF-derived carbonaceous materials enriched with nitrogen: preparation and applications in adsorption and catalysis. Mater. Today 25, 88–111.
Bhadra, B.N., Lee, J.K., Cho, C.-W., Jhung, S.H., 2018. Remarkably efficient adsorbent for the removal of bisphenol A from water: Bio-MOF-1-derived porous carbon. Chem. Eng. J. 343, 225–234.
Cao, J., Yang, Zh., Xiong, Wp., Zhou, Yy., Peng, Yr., Li, X., Zhou, Cy., Xu, R., Zhang, Yr., 2018. One-step synthesis of Co-doped UiO-66 nanoparticle with enhanced removal efficiency of tetracycline: simultaneous adsorption and photocatalysis. Chem. Eng. J. 353, 126–137.
Cao, J., Yang, Z., Xiong, W., Zhou, Y., Wu, Y., Jia, M., Sun, S., Zhou, C., Zhang, Y., Zhong, R., 2020a. Peroxymonosulfate activation of magnetic Co nanoparticles relative to an N-doped porous carbon under confinement: boosting stability and performance. Sep. Purif. Technol. 250, 117237–117246.
Cao, J., Sun, S., Li, X., Yang, Z., Xiong, W., Wu, Y., Jia, M., Zhou, Y., Zhou, C., Zhang, Y., 2020b. Efficient charge transfer in aluminum-cobalt layered double hydroxide derived from Co-ZIF for enhanced catalytic degradation of tetracycline through peroxymonosulfate activation. Chem. Eng. J. 382 122802-112811.
Carabineiro, S.A., Thavorn Amornsri, T., Pereira, M.F., Figueiredo, J.L., 2011. Adsorption of ciprofloxacin on surface-modified carbon materials. Water Res. 45, 4583–4591.
Carabineiro, S.A.C., Thavorn-amornsri, T., Pereira, M.F.R., Serp, P., Figueiredo, J.L., 2012. Comparison between activated carbon, carbon xerogel and carbon nanotubes for the adsorption of the antibiotic ciprofloxacin. Catal. Today 186, 29–34.
Cetecioglu, Z., Ince, B., Gros, M., Rodriguez Mozaz, S., Barcelo, D., Orhon, D., Ince, O., 2013. Chronic impact of tetracycline on the biodegradation of an organic substrate mixture under anaerobic conditions. Water Res. 47, 2959–2969.
Chen, R., Yao, J., Gu, Q., Smeets, S., Baerlocher, C., Gu, H., Zhu, D., Morris, W., Yaghi, O.M., Wang, H., 2013. A two-dimensional zeolitic imidazolate framework with a cushion-shaped cavity for CO_2 adsorption. Chem. Commun. 49, 9500–9502.
Dhakshinamoorthy, A., Asiri, A.M., Garcia, H., 2019. 2D metal-organic frameworks as multifunctional materials in heterogeneous catalysis and Electro/Photocatalysis. Adv. Mater. 31, 1900617–1900656.
Dong, Y., Yu, M., Wang, Z., Zhou, T., Liu, Y., Wang, X., Zhao, Z., Qiu, J., 2017. General synthesis of zeolitic imidazolate framework-derived planar-N-doped porous carbon nanosheets for efficient oxygen reduction. Energy Storage Mater. 7, 181–188.
Gao, Y., Li, Y., Zhang, L., Huang, H., Hu, J., Shah, S.M., Su, X., 2012. Adsorption and removal of tetracycline antibiotics from aqueous solution by graphene oxide. J. Colloid Interface Sci. 368, 540–546.
Huang, L., Zhang, X., Han, Y., Wang, Q., Fang, Y., Dong, S., 2017. In situ synthesis of ultrathin metal–organic framework nanosheets: a new method for 2D metal-based nanoporous carbon electrocatalysts. J. Mater. Chem. A 5, 18610–18617.
Huizar Felix, A.M., Aguilar Flores, C., Martinez de la Cruz, A., Barandiaran, J.M., Sepulveda Guzman, S., Cruz Silva, R., 2019. Removal of tetracycline pollutants by adsorption and magnetic separation using reduced graphene oxide decorated with α-Fe_2O_3 nanoparticles. Nanomaterials 9, 313–326.
Jia, M., Yang, Z., Xu, H., Song, P., Xiong, W., Cao, J., Zhang, Y., Xiang, Y., Hu, J., Zhou, C., Yang, Y., Wang, W., 2020. Integrating N and F co-doped TiO_2 nanotubes with ZIF-8 as photoelectrode for enhanced photo-electrocatalytic degradation of sulfamethazine. Chem. Eng. J. 388, 124388–124400.
Jiang, C., Zhang, X., Xu, X., Wang, L., 2016. Magnetic mesoporous carbon material with strong ciprofloxacin adsorption removal property fabricated through the calcination of mixed valence Fe based metal-organic framework. J. Porous Mater. 23, 1297–1304.
Jiang, Y., Liu, H., Tan, X., Guo, L., Zhang, J., Liu, S., Guo, Y., Zhang, J., Wang, H., Chu, W., 2017. Monoclinic ZIF-8 nanosheet-derived 2D carbon nanosheets as sulfur immobilizer for high-performance Lithium sulfur batteries. ACS Appl. Mater. Interfaces 9, 25239–25249.
Jin, J., Yang, Z., Xiong, W., Zhou, Y., Xu, R., Zhang, Y., Cao, J., Li, X., Zhou, C., 2019. Cu and Co nanoparticles co-doped MIL-101 as a novel adsorbent for efficient removal of tetracycline from aqueous solutions. Sci. Total Environ. 650, 408–418.
Li, S., Zhang, X., Huang, Y., 2017. Zeolitic imidazolate framework-8 derived nanoporous carbon as an effective and recyclable adsorbent for removal of ciprofloxacin antibiotics from water. J. Hazard. Mater. 321, 711–719.
Li, X., Yuan, H., Quan, X., Chen, S., You, S., 2018. Effective adsorption of sulfamethoxazole, bisphenol A and methyl orange on nanoporous carbon derived from metal-organic frameworks. J. Environ. Sci. 63, 250–259.
Liu, Y., 2009. Is the free energy change of adsorption correctly calculated? J. Chem. Eng. Data 54, 1981–1985.
Liu, Z., Tian, J., Zeng, D., Yu, C., Huang, W., Yang, K., Liu, X., Liu, H., 2019. Binary-phase TiO_2 modified Bi_2MoO_6 crystal for effective removal of antibiotics under visible light illumination. Mater. Res. Bull. 112, 336–345.
Low, Z.-X., Yao, J., Liu, Q., He, M., Wang, Z., Suresh, A.K., Bellare, J., Wang, H., 2014. Crystal transformation in zeolitic-imidazolate framework. Cryst. Growth Des. 14, 6589–6598.
Nasir, A.M., Md Nordin, N.A.H., Goh, P.S., Ismail, A.F., 2018. Application of two-dimensional leaf-shaped zeolitic imidazolate framework (2D ZIF-L) as arsenite adsorbent: kinetic, isotherm and mechanism. J. Mol. Liq. 250, 269–277.
Sarker, M., Bhadra, B.N., Seo, P.W., Jhung, S.H., 2017a. Adsorption of benzotriazole and benzimidazole from water over a Co-based metal azolate framework MAF-5(Co). J. Hazard. Mater. 324, 131–138.
Sarker, M., Ahmed, I., Jhung, S.H., 2017b. Adsorptive removal of herbicides from water over nitrogen-doped carbon obtained from ionic liquid@ZIF-8. Chem. Eng. J. 323, 203–211.
Song, P., Yang, Z., Xu, H., Huang, J., Yang, X., Yue, F., Wang, L., 2014. Arsenic removal from contaminated drinking water by electrocoagulation using hybrid Fe–Al electrodes: response surface methodology and mechanism study. Desalin. Water Treat. 57, 4548–4556.
Tang, J., Salunkhe, R.R., Liu, J., Torad, N.L., Imura, M., Furukawa, S., Yamauchi, Y., 2015. Thermal conversion of core-shell metal-organic frameworks: a new method for selectively functionalized nanoporous hybrid carbon. J. Am. Chem. Soc. 137, 1572–1580.
Torad, N.L., Hu, M., Ishihara, S., Sukegawa, H., Belik, A.A., Imura, M., Ariga, K., Sakka, Y., Yamauchi, Y., 2014. Direct synthesis of MOF-derived nanoporous carbon with magnetic Co nanoparticles toward efficient water treatment. Small 10, 2096–2107.
Wang, D., Jia, F., Wang, H., Chen, F., Fang, Y., Dong, W., Zeng, G., Li, X., Yang, Q., Yuan, X., 2018. Simultaneously efficient adsorption and photocatalytic degradation of tetracycline by Fe-based MOFs. J. Colloid Interface Sci. 519, 273–284.
Wang, L., Wen, B., Bai, X., Liu, C., Yang, H., 2019. Facile and green approach to the synthesis of zeolitic imidazolate framework nanosheet-derived 2D Co/C composites for a lightweight and highly efficient microwave absorber. J. Colloid Interface Sci. 540, 30–38.
Wang, H., Yuan, X., Wu, Y., Zeng, G., Dong, H., Chen, X., Leng, L., Wu, Z., Peng, L., 2016. In situ synthesis of In_2S_3@MIL-125(Ti) core–shell microparticle for the removal of tetracycline from wastewater by integrated adsorption and visible-light-driven photocatalysis. Appl. Catal. B 186, 19–29.
Xia, W., Tang, J., Li, J., Zhang, S., Wu, K.C., He, J., Yamauchi, Y., 2019. Defect-rich graphene nanomesh produced by thermal exfoliation of metal-organic frameworks for the oxygen reduction reaction. Angew. Chemie Int. Ed. 58, 13354–13359.
Xiong, W., Zeng, Z., Li, X., Zeng, G., Xiao, R., Yang, Z., Zhou, Y., Zhang, C., Cheng, M., Hu, L., Zhou, C., Qin, L., Xu, R., Zhang, Y., 2018. Multi-walled carbon nanotube/amino-functionalized MIL-53(Fe) composites: remarkable adsorptive removal of antibiotics from aqueous solutions. Chemosphere 210, 1061–1069.
Xiong, W., Zeng, Z., Li, X., Zeng, G., Xiao, R., Yang, Z., Xu, H., Chen, H., Cao, J., Zhou, C., Qin, L., 2019a. Ni-doped MIL-53(Fe) nanoparticles for optimized doxycycline removal by using response surface methodology from aqueous solution. Chemosphere 232, 186–194.
Xiong, W., Zeng, Z., Zeng, G., Yang, Z., Xiao, R., Li, X., Cao, J., Zhou, C., Chen, H., Jia, M., Yang, Y., Wang, W., Tang, X., 2019b. Metal-organic frameworks derived magnetic carbon-αFe/Fe_3C composites as a highly effective adsorbent for tetracycline removal from aqueous solution. Chem. Eng. J. 374, 91–99.
Xu, R., Yang, Z.H., Zheng, Y., Zhang, H.B., Liu, J.B., Xiong, W.P., Zhang, Y.R., Ahmad, K., 2017. Depth-resolved microbial community analyses in the anaerobic co-digester of dewatered sewage sludge with food waste. Bioresour. Technol. 244, 824–835.
Xu, R., Yang, Z.H., Zheng, Y., Wang, Q.P., Bai, Y., Liu, J.B., Zhang, Y.R., Xiong, W.P., Lu, Y., Fan, C.Z., 2019a. Metagenomic analysis reveals the effects of long-term antibiotic pressure on sludge anaerobic digestion and antimicrobial resistance risk. Bioresour. Technol. 282, 179–188.
Xu, X., Ran, F., Fan, Z., Lai, H., Cheng, Z., Lv, T., Shao, L., Liu, Y., 2019b. Cactus-inspired bimetallic metal-organic framework-derived 1D-2D hierarchical Co/N-Decorated carbon architecture toward enhanced electromagnetic wave absorbing performance. ACS Appl. Mater. Interfaces 11, 13564–13573.
Yang, Zh., Cao, J., Chen, Yp., Li, X., Xiong, Wp., Zhou, Yy., Zhou, Cy., Xu, R., Zhang, Yr., 2019. Mn-doped zirconium metal-organic framework as an effective adsorbent for removal of tetracycline and Cr(VI) from aqueous solution. Microporous Mesoporous Mater. 277, 277–285.
Yang, S., Hu, J., Chen, C., Shao, D., Wang, X., 2011. Mutual effects of Pb(II) and humic acid adsorption on multiwalled carbon Nanotubes/Polyacrylamide composites from aqueous solutions. Environ. Sci. Technol. 45, 3621–3627.
Ye, Y., Li, H., Cai, F., Yan, C., Si, R., Miao, S., Li, Y., Wang, G., Bao, X., 2017. Two-dimensional mesoporous carbon doped with Fe–N active sites for efficient oxygen reduction. ACS Catal. 7, 7638–7646.
Yu, J., Xiong, W., Li, X., Yang, Z., Cao, J., Jia, M., Xu, R., Zhang, Y., 2019. Functionalized MIL-53(Fe) as efficient adsorbents for removal of tetracycline antibiotics from aqueous solution. Microporous Mesoporous Mater. 290, 109642–109649.
Zhang, Q.Q., Ying, G.G., Pan, C.G., Liu, Y.S., Zhao, J.L., 2015. Comprehensive evaluation of antibiotics emission and fate in the River Basins of China: source analysis, multimedia modeling, and linkage to bacterial resistance. Environ. Sci. Technol. 49, 6772–6782.
Zheng, F., Yang, Y., Chen, Q., 2014. High lithium anodic performance of highly nitrogen-doped porous carbon prepared from a metal-organic framework. Nat. Commun. 5, 5261–5270.
Zhong, Z., Yao, J., Low, Z.-X., Chen, R., He, M., Wang, H., 2014a. Carbon composite membrane derived from a two-dimensional zeolitic imidazolate framework and its gas separation properties. Carbon 72, 242–249.
Zhong, H.X., Wang, J., Zhang, Y.W., Xu, W.L., Xing, W., Xu, D., Zhang, Y.F., Zhang, X.B., 2014b. ZIF-8 derived graphene-based nitrogen-doped porous carbon sheets as highly efficient and durable oxygen reduction electrocatalysts. Angew. Chemie Int. Ed. 53, 14235–14239.